

A network of parametrically driven silicon nitride mechanical membranes

Luis Mestre,^{1,2} Suyash Singh,^{1,2} Gabriel Margiani,^{1,2} Letizia Catalini,^{1,2,3} Alexander Eichler,^{1,2} and Vincent Dumont^{1,2,*}

¹Laboratory for Solid State Physics, ETH Zürich, 8093 Zürich, Switzerland

²Quantum Center, ETH Zürich, 8093 Zürich, Switzerland

³Center for Nanophotonics, AMOLF, 1098XG Amsterdam, The Netherlands

(Dated: June 9, 2025)

Networks of nonlinear resonators offer a promising platform for analog computing and the emulation of complex systems. However, realizing such networks remains challenging, as it requires resonators with high quality factors, individual frequency tunability, and strong inter-resonator coupling. In this work, we present a system that meets all these criteria. Our system is based on metallized silicon nitride membranes that are coupled via their common substrate and controlled capacitively via electrodes. We demonstrate individual frequency tuning and strong parametric driving of each membrane. Notably, we tune membrane frequencies through avoided crossings and demonstrate tunability of the coupled membrane's parametric response. This platform provides a scalable and controllable setting for exploring collective phenomena, dynamical phase transitions, nonlinear topology, and analog computing.

Introduction.— Networks of coupled oscillators can emulate complex dynamical systems, offering a physical platform to solve computationally hard problems and to explore emergent phenomena in nonequilibrium physics [1–3]. For instance, they can realize Hopfield networks [4] used for novel forms of computing, such as Ising machines [5]. These networks also provide a testbed for studying collective phenomena such as synchronization [6], cascade and critical transitions [7–12], and dynamical phases, e.g. Chimera states [13, 14].

Kerr parametric oscillators (KPOs) are a particularly promising building block for analog computation. A KPO can be realized by modulating the spring constant of a nonlinear resonator at approximately twice its resonance frequency [15–18]. Above a certain modulation threshold, the system transitions into one of two stable oscillation ‘phase states’, each with equal amplitude but opposite phase. These states can be mapped to the classical states of a spin-1/2 system (up and down), and can be used as binary logic elements [19–34] for a variety of applications [35–37]. Additionally, these coupled bimodal and out-of-equilibrium resonators allow for studying complex dynamical phenomena in a highly controllable and stable platform.

While early theory proposals [28, 38, 39] and demonstrations [40] are based on weakly coupled KPOs, much richer physics is found when the coupling strength is on the order of the damping rate [32, 34, 41–43]. There, the interplay between nonlinearity and coupling gives rise to doubly unstable ‘ghost states’ [42] and to additional states with mixed symmetry [34, 41]. Strong coupling is also essential for enabling coherent transitions between states in quantum annealing [44]. Aside from strong coupling, detuning between the constituent oscillators leads to an asymmetric Ising model [33], which is central for

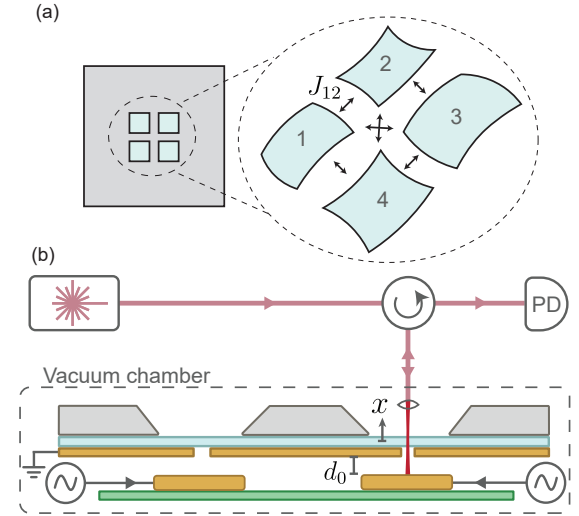


FIG. 1. Coupled silicon nitride membranes. (a) Four silicon nitride mechanical membranes (blue) are coupled through the silicon substrate (gray) to their neighbors with coupling strength J_{ij} . (b) The membranes are metallized and capacitively coupled to electrodes (gold) at a distance $d_0 \approx 13 \mu\text{m}$ below the membranes. We send 1550-nm laser light to a single membrane for interferometric readout. The laser is focused on the membrane with a GRIN lens, and the light reflected from the membrane is picked up by a circulator and collected by a photodiode (PD).

modeling neural networks and other nonreciprocal systems [36, 45]. Combining strong coupling and large *in-situ* tuning in a scalable experimental platform would allow access to a range of important applications, including rapid phase logic operations [24, 25] and programmable neural networks [33]. In reality, however, fulfilling all of these criteria in an experiment is difficult.

In this work, we present an electromechanical platform based on coupled silicon nitride membrane resonators on

* Corresponding author: vdumont@phys.ethz.ch

a single chip. Each resonator can be individually tuned in frequency by a few kHz, features a quality factor up to $Q \sim 10^4$, and exhibits strong nearest-neighbor coupling, with the normal mode splitting comparable or larger than the membranes mechanical linewidth. The experimental platform is scalable, as many membranes can be fabricated on a single silicon substrate. We read out multiple mechanical resonators using a single laser interferometer, significantly reducing the experimental complexity. With this setup, we demonstrate a continuous crossover between a far detuned ‘resonator regime’, with each mode comprising mostly one bare membrane oscillating, to a ‘normal-mode regime’ where we observe strongly hybridized KPOs involving both membranes. The system can thus access various scenarios that have hitherto only been studied separately. In the future, this platform will allow us investigating many-body physics and computational architectures beyond the degenerate Ising system.

Device and readout.— Our device consists of a single silicon chip containing four low-stress silicon nitride membranes (Norcada NXVA-2250-5045A), see Fig. 1(a). The 50 nm-thick membranes have lateral dimensions of $450\mu\text{m} \times 450\mu\text{m}$ and are positioned $50\mu\text{m}$ apart from each other in a two-by-two grid. For electrostatic tuning and actuation, we coat the membranes with Ti (10 nm) and Au (30 nm) using optical lithography and e-beam evaporation, see Fig. 1(b) and Appendix A. The centers of the membranes, where we optically read out the membrane oscillations, are left uncoated to minimize heating due to light absorption. The chip is positioned and clamped on top of spacers on a printed circuit board (PCB), setting a distance $d_0 \approx 13\mu\text{m}$ between the membrane surface and the PCB’s electrodes. The membrane chip and PCB are placed in a vacuum chamber (pressure $\sim 10^{-7}$ mbar) at room temperature.

We read out the motion of a single membrane with an interferometer. Laser light (Rio Orion 1550 nm) with a wavelength of 1550 nm is sent through a fiber to a circulator (Koheron FOCIR1550-A) and into the vacuum chamber with a fiber feedthrough, and couples to free space via an optical fiber end with a 50% reflection coating (Thorlabs, custom made). The 50% transmitted light is focused by a gradient refractive index lens (Thorlabs GRIN2915) onto the uncoated center of the membrane. We measure the total reflected light with a photodiode (PD, Koheron PD100B) and a lock-in amplifier (Zurich Instruments MFLI). The interference between the light reflected from the membrane and from the coated fiber provides a record of the membrane displacement x .

Single membrane resonator.— We first characterize the linear and parametric responses of a single membrane. The other membranes being far detuned in frequency, we observe the motion of the mode consisting mostly of the membrane we read out. We consider the displacement x_i of the fundamental out-of-plane vibration mode of mem-

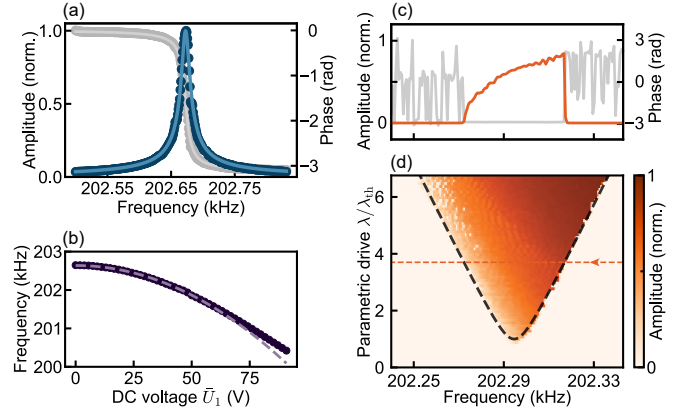


FIG. 2. Characterization of single membrane resonator. (a) Measured (dots) and fitted (solid lines) mechanical response amplitude (blue) and phase (grey) as a function of the driving frequency ω . Fitting to the resonance curve $x_1(\omega) \propto (\omega_1^2 - \Omega^2 - i\omega\Gamma_1)^{-1}U_1(\omega)$ yields $\Omega_1/2\pi \approx 202.67$ kHz and damping $\Gamma_1/2\pi = (12.59 \pm 0.08)$ Hz. (b) Membrane frequency $\Omega_1 + \delta\Omega_1$ as a function of applied DC voltage \bar{U}_1 . From a quadratic fit, we extract the membrane-electrode distance $d_0 \approx 13\mu\text{m}$, see Appendix C. (c) Amplitude (orange) and phase (grey) measured at ω in response to parametric driving at 2ω with $\lambda/\lambda_{th} = 3.7$. Inside the large-amplitude lobe, the phase locks to one of the two phase states. (d) Repeating frequency sweeps for multiple λ/λ_{th} reveals the characteristic ‘Arnold tongue’. The sweep in (c) is marked by a dashed orange line. A black dashed line marks the boundary of the Arnold tongue, using the fitted value from the linear sweep.

brane i , modeled by the resonator equation of motion

$$\ddot{x}_i + \Omega_i^2 [1 - \lambda_i \cos(2\omega t)]x_i + \Gamma_i \dot{x}_i + \beta_i x_i^3 + \sum_{j \neq i} J_{ij}^2 x_j = F_i(t)/m_i, \quad (1)$$

where dots indicate derivation with respect to time t , Ω_i is the resonance frequency, Γ_i the damping rate, β_i the geometrical Duffing nonlinearity, and $J_{ij} = J_{ji}$ the coupling rate to membrane j . The coupling J_{ij} can be tuned by varying the distance between the membranes. The resonator is driven by a near-resonant force $F_i = \tilde{F}_i \cos(\omega t)$ with $\omega \approx \Omega_i$, and a parametric drive with modulation depth λ_i . The effective mass $m_i \approx 38$ ng of each membrane is estimated from the thicknesses of the silicon nitride and the metal layers, see Appendix B.

We measure the linear response of membrane 1 by applying a voltage $U_1 = \bar{U}_1 + \tilde{U}_{\omega,1} \cos(\omega t)$ to the electrode underneath the membrane, with \bar{U}_1 a DC voltage, and $F_1 \propto \tilde{U}_{\omega,1} \cos(\omega t)$. We measure the complex mechanical response $x_1(\omega)$ while sweeping ω , see Fig. 2(a). For small enough $\tilde{U}_{\omega,1}$ and $\lambda_1 = 0$, the response is small and we can approximate $\beta_1 x_1^3 = 0$. From a fit to the measured response, we extract a fundamental mode frequency $\Omega_1/2\pi = 202.67$ kHz and decay rate $\Gamma_1/2\pi = (12.59 \pm 0.08)$ Hz, yielding a quality factor $Q_1 \equiv \Omega_1/\Gamma_1 = (16.1 \pm 0.1) \times 10^3$. For these

measurements, all the other membranes are far detuned in frequency, so there is barely any mode hybridization. In a similar fashion, we characterize membrane 2, finding a resonance frequency $\Omega_2/2\pi \approx 203.40$ kHz, a decay rate $\Gamma_2/2\pi = (39.2 \pm 0.6)$ Hz, and a quality factor $Q_2 = (5.19 \pm 0.08) \times 10^3$, see Appendix D. We normalize all measured amplitude due to the difficulty of calibrating from voltage to position in our apparatus, see Appendix E.

The voltage U_i can also be used to tune each membrane frequency Ω_i [46–49]. This voltage generates a capacitive force $F_{c,i}$ which leads to an electrical spring constant $k_{c,i} = -\partial F_{c,i}/\partial x_i = U_i^2 \partial^2 C_i / \partial x_i^2$, where the electrode-membrane capacitance C_i is inversely proportional to their separation, $C_i \propto (d_0 + x_i)^{-1}$, see Appendix C. This shifts $\Omega_i = \sqrt{k_i/m_i}$ by

$$\delta\Omega_i = \sqrt{\frac{k_i + k_{c,i}}{m_i}} - \sqrt{\frac{k_i}{m_i}} \approx \frac{1}{4m_i\Omega_i} \frac{\partial^2 C_i}{\partial x_i^2} U_i^2, \quad (2)$$

in the limit $k_{c,i} \ll k_i$, with k_i the bare mechanical spring constant of the membrane. In Fig. 2(b), we show Ω_1 being tuned by a DC voltage \bar{U}_1 . Up to 50 V, we observe the quadratic dependency $\delta\Omega_1 \propto \bar{U}_1^2$ expected from Eq. (2), with a tunability of $\delta\Omega_1 > 2$ kHz. At higher \bar{U}_1 , the frequency shift does not follow Eq. (2) precisely. We suspect this stiffening to be caused by the positive Duffing nonlinearity at large equilibrium positions, see Appendix C.

We drive the membrane parametrically by applying both a DC voltage \bar{U}_i and a time-varying (AC) voltage at frequency 2ω with amplitude $\tilde{U}_{2\omega,i}$, while we set $F_1 = 0$ (i.e., there is no voltage at frequency ω). With a total voltage $U_i(t) = \bar{U}_i + \tilde{U}_{2\omega,i} \cos(2\omega t)$ and using Eq. (2) for $\bar{U}_i \gg \tilde{U}_{2\omega,i}$, we approximate the induced frequency shift as

$$\delta\Omega_i(t) \approx \frac{1}{4m_i\Omega_i} \frac{\partial^2 C_i}{\partial x_i^2} \left[\bar{U}_i^2 + \bar{U}_i \tilde{U}_{2\omega,i} \cos(2\omega t) \right], \quad (3)$$

with the second term corresponding to an effective $\lambda \propto \tilde{U}_{2\omega,i}$ in Eq. (1). We record the membrane's oscillation amplitude and phase while slowly sweeping ω from high to low frequencies, i.e., in the direction opposed to the Duffing nonlinearity, see Fig. 2(c). Within a frequency window around Ω_1 , we observe parametric oscillations with large amplitude (limited by β_1) and a phase locked to one of the two phase states (differing by phase π) [18]. Outside the window, the response amplitude is zero and the phase is undefined. Repeating parametric sweeps for various values of $\tilde{U}_{2\omega,1}$, we obtain an ‘Arnold tongue’, see Fig. 2(d). We label the vertical axis by the normalized quantity $\lambda/\lambda_{\text{th}}$, where λ_{th} is the threshold value above which parametric oscillations are measured within a frequency sweep. This phase diagram indicates the region where the response is finite and the KPO is in one of the two phase states.

Coupled membranes.— We now probe the response of two neighboring membranes (1 and 2), coupled through

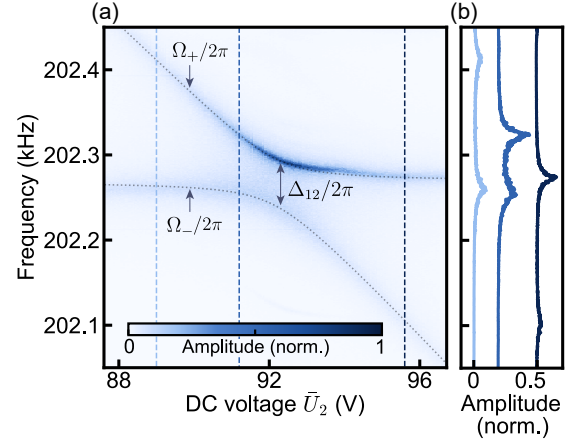


FIG. 3. Avoided crossing between the fundamental modes of membranes 1 and 2. (a) Displacement amplitude spectral density (ASD) of membrane 1 as a function of frequency and \bar{U}_2 applied to membrane 2, with fixed $\bar{U}_1 = 34.1$ V. Dotted lines indicate fits of $\Omega_{\pm}/2\pi$, yielding an avoided crossing gap $\Delta_{12}/2\pi = (55.2 \pm 0.5)$ Hz, cf. Eq. (4). (b) Displacement ASD line cuts for different values of \bar{U}_2 , corresponding to the vertical dashed lines in panel (a). The amplitudes are offset for better visibility.

their substrate [50–52] and tuned by separate DC voltages $\bar{U}_{1,2}$. From Eq. (1), we find the system's eigenfrequencies, see Appendix F,

$$\Omega_{\pm} = \left[\frac{\Omega_1^2 + \Omega_2^2}{2} \pm \frac{\sqrt{(\Omega_1^2 - \Omega_2^2)^2 + 4J_{12}^4}}{2} \right]^{1/2}, \quad (4)$$

which, for $\Omega_1 \approx \Omega_2$ and in the limit $J_{12} \ll \Omega_1$, simplifies to $\Omega_{\pm} = \Omega_1 \mp J_{12}^2/(2\Omega_1)$. This yields a characteristic avoided crossing with a gap $\Delta_{12} \equiv \Omega_- - \Omega_+ = J_{12}^2/\Omega_1$. The + (−) mode corresponds to the symmetric (anti-symmetric) mode $x_1 + x_2$ ($x_1 - x_2$). To measure this gap, we keep $\bar{U}_1 = 34.1$ V constant and measure the spectral response of membrane 1 to a white force noise for various values of \bar{U}_2 , see Fig. 3.

Fitting Eq. (4) to our data, we obtain a coupling $J_{12}/(2\pi) = (3.34 \pm 0.03)$ kHz and splitting $\Delta_{12}/2\pi = J_{12}^2/(2\pi\Omega_1) = (55.2 \pm 0.5)$ Hz. This splitting is on the order of the combined membranes' mechanical linewidth $(\Gamma_1 + \Gamma_2)/2\pi = (51.8 \pm 0.7)$ Hz. With an analogous measurement, we characterize the coupling between membrane 1 and its diagonally opposed membrane 3 to be $J_{13}/(2\pi) = (2.77 \pm 0.03)$ kHz, with normal mode splitting $\Delta_{13}/2\pi = (37.9 \pm 0.4)$ Hz, see Appendix G. As expected, this coupling is smaller due to the larger separation between those two membranes.

So far, we have shown that our system of membrane resonators has mechanical modes with high quality factors whose frequencies can be widely tuned and whose coupling is on the order of the total damping rate. We have also seen that these modes individually respond to parametric driving. Now, we combine all of these elements, demonstrating a network of KPOs that can be

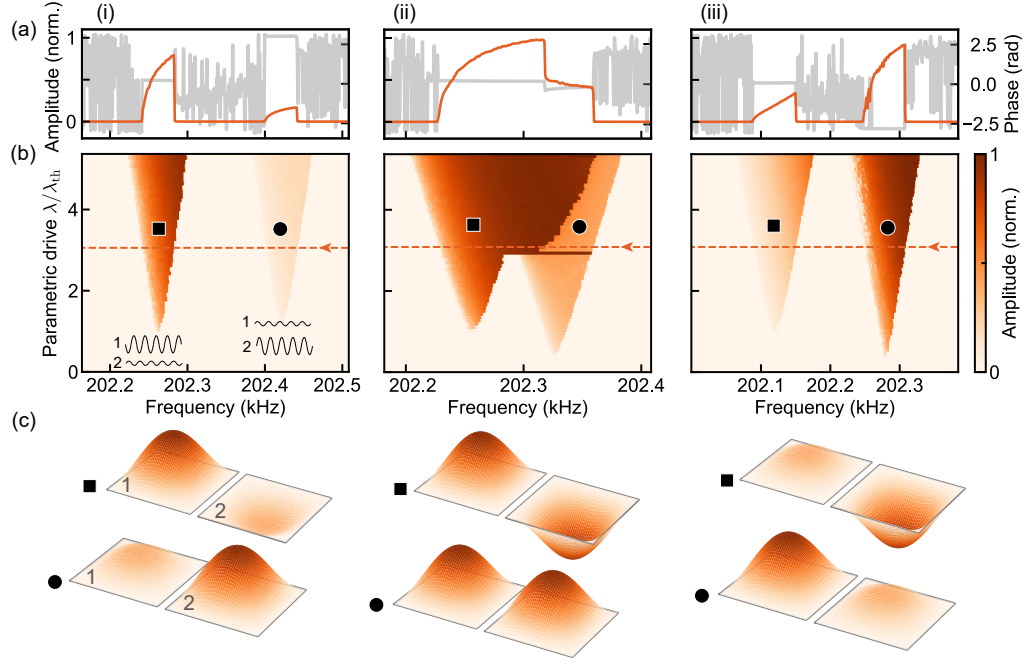


FIG. 4. Parametric response of two coupled membranes (1 and 2). Columns (i)-(iii) correspond to three different values of \bar{U}_2 , cf. vertical lines in Fig. 3. (a) Amplitude (orange) and phase (gray) measured on membrane 1 with $\lambda/\lambda_{th} = 3.1$ and $\bar{U}_1 = 34.1$ V. The frequency was swept from high to low values. (b) Response to parametric driving of the coupled membranes for various λ/λ_{th} . The data in (a) was taken along the dashed orange lines. An inset in panel (i) illustrates x_1 and x_2 as a function of time. (c) Qualitative mode shape of each membrane when driven at the positions in (b) indicated by the square and circle shapes.

continuously tuned between two very different regimes: in the first regime, the original membrane resonators (1 and 2) are detuned, and the system response can be well understood in terms of parametric oscillations localized on either membrane. In the second regime, the resonators form hybridized modes and the parametric response involves both membranes simultaneously, generating a rich phase diagram of overlapping Arnold tongues.

In Fig. 4, we parametrically drive the two membranes simultaneously with strength λ and frequency 2ω while measuring the amplitude and phase of membrane 1 at ω . For each measurement, we set $F_i = 0$ and apply fixed DC voltages \bar{U}_1 and \bar{U}_2 to the two membranes. We select three different values for \bar{U}_2 , corresponding to three different points along the avoided crossing, see vertical lines in Fig. 3(a). Sweeping ω from higher to lower frequencies, we obtain Fig. 4(a). Repeating the parametric drive sweeps for multiple values of λ , we recover the colorplots in Fig. 4(b). Note that the AC voltage amplitudes sent to each membrane needs to be tuned to compensate for mode hybridization and difference in quality factors, see Appendix H.

In Figs. 4(i) and (iii), we measure two tongue-shaped regions with finite amplitudes and defined phases. The tongues are centered around the two mode frequencies measured for the corresponding voltages in Fig. 3, with the tongue around Ω_1 exhibiting a stronger signal than that at Ω_2 . We interpret these results the following way:

here, the two membranes are detuned from each other, and we predominantly drive only one of them at each frequency. This produces large oscillations of membrane 1 around 202.26 kHz in Fig. 4(i) and around 202.28 kHz in Fig. 4(iii). Weak oscillations of membrane 1 can still be seen in the other tongue around 202.41 kHz in Fig. 4(i) and around 202.12 kHz in Fig. 4(iii). This is due to the off-resonant force it experiences through the coupling term $J_{12}^2 x_2$ in the presence of parametric oscillation of membrane 2, cf. Eq. (1). Inset in Fig. 4(i)(b) illustrate x_1 and x_2 as a function of time for the different lobes, while visualizations of the spatial mode shapes are shown in Fig. 4(c).

When the membrane resonators are tuned into an avoided crossing, they become hybridized. Parametrically driving these normal modes results in a pattern of overlapping Arnold tongues [41]. The Arnold tongues with lower and higher center frequency represent anti-symmetric ($x_1 - x_2$) and symmetric ($x_1 + x_2$) parametric oscillation states, respectively, see Appendix F. Transitions between states can be measured as jumps in the oscillation amplitude. For the line sweep in Fig. 4(a)(ii), a jump to the symmetric state occurs at approximately 202.35 kHz, below which the zero-amplitude state becomes unstable and parametric oscillations start. A second jump is observed at 202.32 kHz, well within the symmetric Arnold tongue.

To the left of this jump, the interplay between the non-

linearity and the resonator coupling destabilizes the symmetric state, forcing the system to jump to the antisymmetric state [41, 43]. Those intricate patterns were previously only measured with electrical resonators whose quality factors were much lower than those of the mechanical modes reported here [32, 34, 41]. Confirming their existence in a high- Q system is a first step towards studying many-body fluctuations [53] and inter-state statistical transitions [42] in nanomechanical systems. Such dynamics can be measured with a lock-in amplifier when a mode's ringdown time ($2Q/\Omega_i$) is longer than the required integration time τ . With electrical systems, which typically have ringdown times on the order of 25 μ s [25], this requirement is harder to fulfill than in the present system, which features $\tau_1 = 2Q_1/\Omega_1 \approx 26$ ms and $\tau_2 = 2Q_2/\Omega_2 \approx 8$ ms.

We emphasize that even though we only measure the amplitude and phase of membrane 1, we gain access to much information about the entire coupled system. In the detuned case in Fig. 4(i) and (iii), the coupling allows us to indirectly measure the parametric oscillation of membrane 2 via the motion of membrane 1. In Fig. 4(ii), we can detect transitions between different parametric oscillation states of the network via jumps in the amplitude. Together with analytical and numerical modeling [41, 43], such data enables us to understand the underlying phase diagram of the KPO network, i.e., which oscillation states exist where in the space spanned by ω and λ . The amplitude can then be used as a proxy measurement to differentiate between different states, for example in the context of KPO-based Ising simulators [34]. To calibrate and directly confirm such experiments, our setup could be combined with wide-field stroboscopic imaging to measure the displacement of all the membranes simultaneously [54].

Summary and outlook.— We demonstrated a system of coupled nonlinear mechanical resonators based on silicon nitride membranes. Coupling between membranes can be designed via their separation. The platform combines high quality factors and large individual tuning of the resonator frequencies, offering access to distinct regimes of dynamics. In addition, we show that information about the entire network can be inferred from a measurement of just one membrane.

This platform is easily scalable. We envision that networks of six or nine membrane resonators can be probed without significant additional technical overhead, assuming that existing theory models [43] appropriately describe the emerging phenomena. Beside the number of membranes, the quality factors of individual membranes can potentially be increased by orders of magnitudes using soft clamping [55, 56]. This will greatly facilitate the study of activated fluctuations between the different states in such complex systems [42]. When detuning the constituent KPOs, the system could potentially mimic an asymmetric Ising model, which is central to the understanding of neural networks [33]. Furthermore, we plan to use this platform as a testbed for Ising ma-

chines [5], Hopfield networks [4], and the study of emergent nonlinear collective phenomena [6–12], dynamical phases [13, 14], and topology in nonlinear networks [57–59]. With this, nanomechanical KPO networks will become a useful tool for tackling open questions in complex systems and artificial neural networks.

Acknowledgments.— We thank R. Pachlatko, L. Ziegler, and N. Prumbaum for insightful discussions. V.D. acknowledges support from the ETH Zurich Postdoctoral Fellowship Grant No. 23-1 FEL-023 and the Swiss National Science Foundation (SNSF) Postdoctoral Fellowship Grant 217118. A.E. acknowledges financial support from the Swiss National Science Foundation (SNSF) through the Sinergia Grant No. CR-SII5.206008/1.

Appendix A: Membrane metallization

We metallize the silicon nitride membranes for capacitive actuation, see Fig. 5(a). All the membranes are coated with titanium (for adhesion) and gold (for electrical conduction), and connected to a common ground. We leave the center of each membrane uncoated in order to reduced laser absorption which we found to lead to large mechanical frequency shifts (kilohertz-scale mechanical resonance shifts for milliwatt-level laser power). The electrodes on the PCB allow to individually address each membrane.

To metallize the membranes, we first attach the 5 mm \times 5 mm silicon chip to a silicon wafer with Crystal bond. We spincoat 450 nm of photosensitive liftoff resist (LOR5B) for 40 s at 4000 rpm, followed by a 300 s bake-out on a hot plate at 170 $^{\circ}$ C. We then spincoat a 1.8 μ m thick layer of the photoresist AZ1518 (40 s spinning at 4000 rpm and bake-out for 90 s at 100 $^{\circ}$ C). We define a pattern by laser writing (Heidelberg DWL66+) with a laser wavelength 375 nm, write speed 110 mm²/min, and laser power 55 μ W. We then develop the two resists in AZ400k for 2 mins. We transfer the sample to deionized water, and then dry it with a nitrogen gun. We further clean leftover resist residues in an O₂ asher for 120 s at 100 W. After this process, we detach the membrane from the silicon holder by placing it on a hotplate at 70 $^{\circ}$ C. We use e-beam evaporation to deposit 10 nm of Ti followed by 30 nm of Au. We lift off the remaining resist by placing the device in a dimethyl sulfoxide (DMSO) bath at 80 $^{\circ}$ C for 30 mins. Finally, we rinse and clean the device with acetone, isopropyl alcohol (IPA) and deionized (DI) water, and blow it dry with a nitrogen gun. The membrane chip is then clamped to the PCB, see Fig. 5(b).

Appendix B: Membrane effective mass

Each membrane consists of a 50-nm-thick silicon nitride film (density 3170 kg/m³), coated with a 10 nm thick titanium layer (density 4506 kg/m³) and a 30 nm

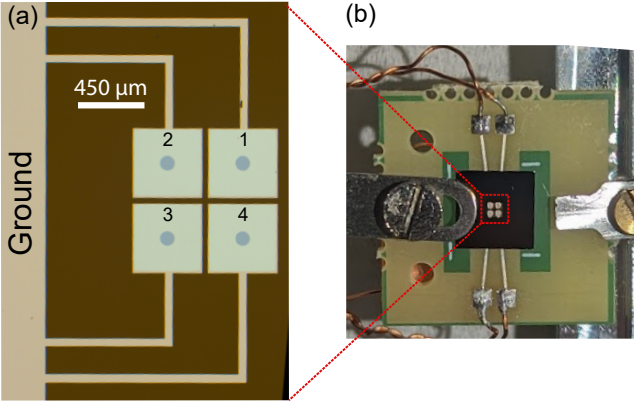


FIG. 5. Parametric membranes device. (a) Microscope image of the metallized membranes with labels 1-4. All membranes share a common ground and have their center uncoated. (b) Photograph of the membrane chip after it is clamped to the PCB.

thick gold layer (density $19\,300\text{ kg/m}^3$) [60]. The silicon nitride has an area of $(0.45\text{ mm})^2 = 0.20\text{ mm}^2$, while the metal coatings cover a slightly smaller area of 0.19 mm^2 due to the central hole with a radius of $50\text{ }\mu\text{m}$. Summing the masses of these layers gives a total mass of approximately 150 ng . The effective mass of the fundamental mode is approximately a quarter of this total mass [61], i.e., $m \approx 38\text{ ng}$.

Appendix C: Capacitive driving

Here, we calculate the capacitive force $F_{c,i}$ and the effective spring constant $k_{c,i}$ induced on membrane i by applying a voltage U_i on the electrode beneath it.

Capacitance: We consider the capacitance between two conducting plates of area $A = (450\text{ }\mu\text{m})^2$, i.e. the membrane and electrode metallization area (neglecting the metallization hole of radius $50\text{ }\mu\text{m}$), which are separated by a distance d_i . This leads to capacitance

$$C_i = \epsilon_0 \epsilon_r \frac{A}{d_i}, \quad (\text{C1})$$

with $\epsilon_0 = 8.85 \times 10^{-12}\text{ F/m}$ the vacuum permittivity, and $\epsilon_r = 1$ the relative permittivity of the surrounding medium (vacuum).

We need to take into account the fundamental membrane mode-shape $u(y, z)$ in the y - z membrane plane, which is [62]

$$u(y, z) = \sin\left(\frac{\pi y}{L}\right) \sin\left(\frac{\pi z}{L}\right), \quad (\text{C2})$$

assuming clamped boundary conditions for the membrane and with $L = 450\text{ }\mu\text{m}$ the membrane lateral dimension. In this paper, we only consider the fundamental mode of each membrane, but a similar analysis can be

done for higher order mechanical modes. The membrane-electrode separation is $d_i(y, z) \equiv d_0 + u(y, z)x_i$, with d_0 the distance between the membrane and the electrode, and x_i the membrane displacement at its center. The capacitance is then [49]

$$C_i = \int_0^L \int_0^L \frac{\epsilon_0 \epsilon_r}{d_0 + u(y, z)x_i} dy dz. \quad (\text{C3})$$

Capacitive force: The potential energy of the capacitor is $U_{\text{pot},i} = -C_i U_i^2/2$ for a voltage U_i applied to the membrane's electrode, yielding an attractive force

$$F_{c,i}(x_i) = -\frac{\partial U_{\text{pot},i}}{\partial x_i} = \frac{1}{2} \frac{\partial C_i}{\partial x_i} U_i^2 \quad (\text{C4})$$

$$= -\frac{1}{2} U_i^2 \int_0^L \int_0^L \frac{\epsilon_0 \epsilon_r u(y, z)}{[d_0 + u(y, z)x_i]^2} dy dz. \quad (\text{C5})$$

Spring constant: At the equilibrium position x_{eq} , this force can be approximated as

$$F_{c,i}(x_i) \approx F_{c,i}(x_{\text{eq}}) + (x_i - x_{\text{eq}}) \left. \frac{\partial F_{c,i}}{\partial x_i} \right|_{x_i=x_{\text{eq}}}, \quad (\text{C6})$$

for $x_i \ll d_0$. When inserted in the equations of motion, the second term leads to a capacitive spring constant

$$k_{c,i} = - \left. \frac{\partial F_{c,i}}{\partial x_i} \right|_{x_i=x_{\text{eq}}} \quad (\text{C7})$$

$$= -U_i^2 \int_0^L \int_0^L \frac{\epsilon_0 \epsilon_r u^2(y, z)}{[d_0 + u(y, z)x_{\text{eq}}]^3} dy dz, \quad (\text{C8})$$

generating a spring softening. In the limit of small changes in equilibrium position, $x_{\text{eq}} \ll d_0$, the spring constant becomes

$$k_{c,i} \approx -\frac{\epsilon_0 \epsilon_r}{d_0^3} U_i^2 \int_0^L \int_0^L u^2(y, z) dy dz \quad (\text{C9})$$

$$= -\frac{\epsilon_0 \epsilon_r A}{4d_0^3} U_i^2. \quad (\text{C10})$$

Frequency shift: As mentioned in the main text, $k_{c,i}$ is an additional spring constant acting on the mechanical resonator, leading to an effective spring constant $k_i + k_{c,i}$ and a shifted mechanical frequency $\Omega_{\text{eff},i} = \sqrt{(k_i + k_{c,i})/m_i}$. The mechanical frequency shift is

$$\delta\Omega_i = \Omega_{\text{eff},i} - \Omega_i = \sqrt{\frac{k_i + k_{c,i}}{m_i}} - \sqrt{\frac{k_i}{m_i}}, \quad (\text{C11})$$

which, in the limit of $k_{c,i} \ll k_i$, reduces to

$$\delta\Omega_i \approx \frac{k_{c,i}}{2m_i\Omega_i} = -\frac{\epsilon_0 \epsilon_r A}{8m_i\Omega_i d_0^3} U_i^2. \quad (\text{C12})$$

Thus, the frequency of the resonator decreases quadratically with voltage U_i applied to the electrode underneath it.

Membrane-electrode distance: Equation (C12) provides a way of extracting the membrane-electrode distance d_0 . Using the membrane area $A = 0.2 \text{ mm}^2$, the effective mass $m_i \approx 38 \text{ ng}$ derived in Appendix B, and the prefactor $B \equiv -\epsilon_0 \epsilon_r A / (8m_i \Omega_i d_0^3) = 2\pi \times (0.309 \pm 0.001) \text{ Hz/V}^2$ from the fit in Fig. 2(b) relating the change in mechanical frequency for an applied voltage \bar{U}_i , we obtain $d_0 \approx 13 \mu\text{m}$. At that distance, the membrane-electrode capacitance is $C_i \approx 140 \text{ fF}$.

Equilibrium position: We note that the first term, i.e. $F_{c,i}(0)$, in eq. (C6) leads to a shift of the membrane's equilibrium position to $x_{\text{eq},i}$, which can cause an increased mechanical frequency (stiffening) due to the positive Duffing nonlinearity βx_i^3 . To see this, we first find the equilibrium position $x_{\text{eq},i}$ where $F_{c,i}(0) - m_i \Omega_i^2 = 0$,

$$x_{\text{eq}} = -\frac{1}{2m_i \Omega_i^2} \frac{\partial C_i}{\partial x_i} U_i^2 \approx -\frac{2\epsilon_0 \epsilon_r A}{\pi^2 m_i \Omega_i^2 d_0^2} U_i^2 \quad (\text{C13})$$

in the limit $x_i \ll d_0$, and using $\partial C_i / \partial x_i = 4\epsilon_0 \epsilon_r A / (\pi^2 d_0^2)$.

We can redefine x_i around this equilibrium position $x_i \rightarrow x_{\text{eq},i} + x_i$, the Duffing term βx_i^3 then becomes

$$\beta(x_{\text{eq},i} + x_i)^3 = \beta x_{\text{eq},i}^3 + 3\beta x_{\text{eq},i}^2 x_i + 3\beta x_{\text{eq},i} x_i^2 + \beta x_i^3. \quad (\text{C14})$$

The first term $\beta x_{\text{eq},i}^3$ leads to a shift in equilibrium position, the second term $3\beta x_{\text{eq},i}^2 x_i$ to a spring constant shift $3\beta x_{\text{eq},i}^2$, the third term $3\beta x_{\text{eq},i} x_i^2$ to a static force and dynamics at 2ω for $x_i \sim \cos(\omega t)$, which gets filtered out by measuring with our lock-in at frequency ω [63] and effectively leads to a renormalization of the Duffing nonlinearity [64, 65], and the fourth term $3\beta x_i^3$ to the usual Duffing nonlinearity.

Appendix D: Characterization of membranes 2 and 3

Here, we characterize the linear and parametric responses of membranes 2 and 3.

Linear responses: To directly read out the motion of membrane $i = \{2, 3\}$, we first move the laser to the center of the corresponding membrane. Then, similarly as in the main text, we measure the linear response of membrane i by applying a voltage $U_i = \bar{U}_i + \tilde{U}_{\omega,i} \cos(\omega t)$ to the electrode beneath it and by directly measuring its displacement amplitude $|x_i(\omega)|$ and phase $\arg\{x_i(\omega)\}$ at that same frequency. We detune the membranes which are close in frequency by applying a DC voltage to them. We present this measurement for membrane 2 in Fig. 6(a), and for membrane 3 in Fig. 6(b). From the resonance fit, we extract for membrane 2 a frequency $\Omega_2/2\pi \approx 203.40 \text{ kHz}$ and a damping rate $\Gamma_2/2\pi = (39.2 \pm 0.6) \text{ Hz}$, yielding a quality factor $Q_2 = (5.19 \pm 0.08) \times 10^3$. For membrane 3, we extract a frequency $\Omega_3/2\pi \approx 203.37 \text{ kHz}$ and a damping rate $\Gamma_3/2\pi = (49 \pm 2) \text{ Hz}$, yielding a quality factor $Q_3 = (4.1 \pm 0.2) \times 10^3$. The uncertainty on

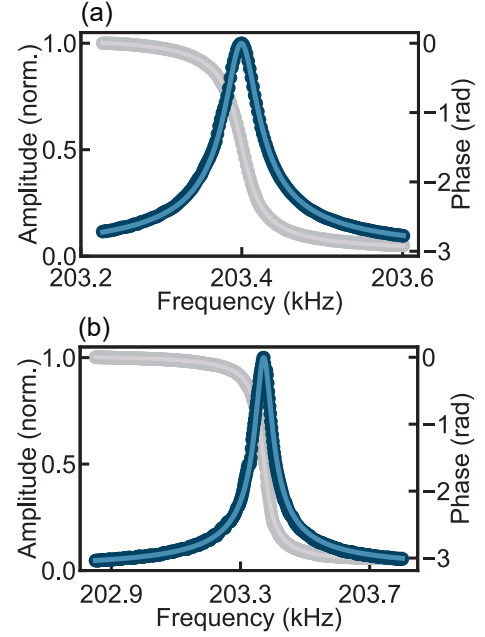


FIG. 6. Linear mechanical response of membranes 2 and 3. Measured (dots) and fitted (solid lines) mechanical response amplitude (blue) and phase (grey) as a function of the driving frequency ω for (a) membrane 2 and (b) membrane 3. From the fits, we extract the frequency $\Omega_2/2\pi \approx 203.40 \text{ kHz}$ and damping rate $\Gamma_2/2\pi = (39.2 \pm 0.6) \text{ Hz}$ (quality factor $Q_2 = (5.19 \pm 0.08) \times 10^3$) of membrane 2, and the frequency $\Omega_3/2\pi \approx 203.37 \text{ kHz}$ and damping rate $\Gamma_3/2\pi = (49 \pm 2) \text{ Hz}$ (quality factor $Q_3 = (4.1 \pm 0.2) \times 10^3$) of membrane 3.

the fitted values of the frequencies are on the order of $\sim 10 \text{ mHz}$, which is much smaller than the $\sim 10 \text{ Hz}$ drifts we typically see in our experiment (for a fixed laser power and position).

Parametric responses: To measure the parametric response of membrane $i = \{2, 3\}$, we first position the laser on the corresponding membrane. Then, we apply a voltage $U_i(t) = \bar{U}_i + \tilde{U}_{2\omega,i} \cos(2\omega t)$, and read out the response $x_i(\omega)$ at frequency ω while sweeping ω from high to low frequencies. Doing so for a fixed parametric drive strength $\lambda \propto \tilde{U}_{2\omega,i}$, we obtain the top panels in Fig. 7(i) and Fig. 7(ii), for membrane 2 and 3, respectively. Note that the readout in this measurement at large parametric drive is highly nonlinear. This is because the amplitude of the motion x_i is enough to bring the membrane motion over a minimum or maximum of the interference fringe, i.e. $|x_i| \gtrsim 1550 \text{ nm}/8$. When looking from high to low frequencies at the parametric sweeps at large parametric drives, e.g. top panels of Fig. 7(a), after the “jump” in the parametric response, the parametric response first increases and then decreases instead of simply decreasing due to this optical readout nonlinearity.

Repeating this measurement for various parametric drive strengths λ , we obtain the Arnold tongues shown in Fig. 7(b). The outline of the Arnold tongue is given

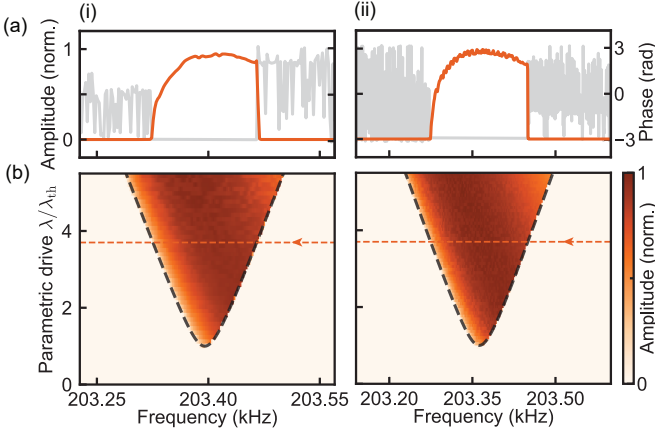


FIG. 7. Parametric sweeps of (i) membrane 2 and (ii) membrane 3. (a) Amplitude (orange) and phase (grey) responses for a single parametric sweeps with $\lambda/\lambda_{\text{th}} = 3.7$. (b) Arnold tongues obtained by repeating the parametric sweeps for various λ . The black dashed outlines is the fit of Eq. (D2) to our data, with damping values obtained from the linear responses, see Fig. 6, and with the frequencies as the only fit parameter, to account for the added DC voltage for the parametric sweep measurements and frequency fluctuations. The sweeps in (a) are marked by dashed orange lines.

by [18]

$$\lambda_i = 2\sqrt{\frac{\Gamma_i^2 \omega^2}{\Omega_i^4} + \left(1 - \frac{\Omega_i^2}{\omega^2}\right)^2}, \quad (\text{D1})$$

which can be expressed as

$$\frac{\lambda_i}{\lambda_{\text{th}}} = \sqrt{\frac{\omega^2}{\Omega_i^2} + \left(1 - \frac{\omega^2}{\Omega_i^2}\right)^2 \frac{\Omega_i^2}{\Gamma_i^2}} \quad (\text{D2})$$

with a parametric threshold $\lambda_{\text{th},i} = 2/Q_i = 2\Gamma_i/\Omega_i$.

Appendix E: Normalized displacement amplitudes

In the main text, all measured amplitudes $|x_i|$ are presented normalized. The laser light not only reflects from the membrane, but also from the PCB. This forms two low-finesse interferometers, akin to a membrane inside an optical cavity [66–68]: (1) between the GRIN lens and the membrane, and (2) between the membrane and the PCB. To calibrate for this displacement, we would have to displace the membrane by a quarter of the laser wavelength, which we cannot do in our current setup. In future experiments, we will add a piezoelectric actuator to move the membrane. Alternatively, thermomechanical motion could be used for calibration, but we cannot assume thermal equilibrium due to noise in our voltage source.

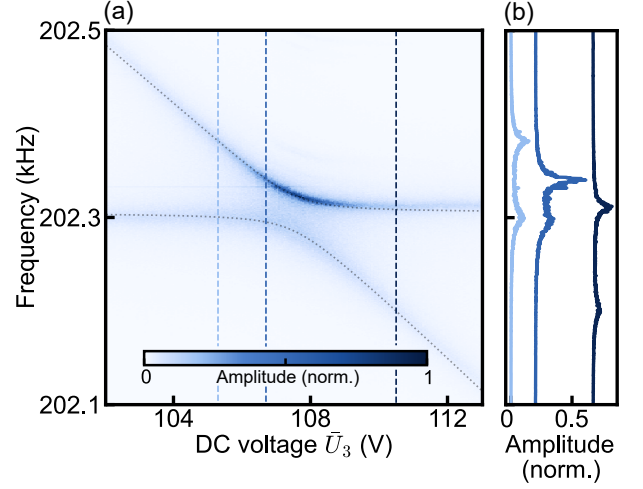


FIG. 8. Avoided crossing between membranes 1 and 3. (a) Displacement amplitude spectral density of membrane 1 as a function of frequency and \bar{U}_3 applied to membrane 3, with fixed $\bar{U}_1 = 34.1$ V. Dotted lines indicate fits of $\Omega_{\pm}/2\pi$, using Eq. (4), yielding coupling $J_{13}/2\pi = (2.77 \pm 0.03)$ kHz and an avoided crossing gap $\Delta_{13}/2\pi = (37.9 \pm 0.4)$ Hz. (b) Displacement ASD line cuts for different values of \bar{U}_3 , corresponding to the vertical dashed lines in panel (a).

Appendix F: Avoided crossing model

In this appendix, we derive the eigenmodes of two coupled membranes. Starting with the coupled equation of motions given by Eq. (1), and assuming that the membranes have the same effective mass $m_i = m_j = m$ and symmetric coupling $J_{ij} = J_{ji}0$, we have the oscillator equations of motion

$$\ddot{x}_i + \Omega_i^2 x_i + J_{ij}^2 x_j = 0, \quad (\text{F1})$$

$$\ddot{x}_j + \Omega_j^2 x_j + J_{ji}^2 x_i = 0. \quad (\text{F2})$$

Here, we set $\beta x_i^3 = \beta x_j^3 = 0$ and $\Gamma_i = \Gamma_j = 0$ since we are only interested in the eigenmodes frequencies and in their composition in the linear regime. Defining the displacement vector, $\mathbf{x} = (x_i, x_j)^T$, with T denoting transpose, this equation can be rewritten in a compact form as

$$(\mathbf{A} - \omega^2 \mathbf{I}_2) \mathbf{x} = 0, \quad (\text{F3})$$

where $\mathbf{I}_2 = \text{diag}(1, 1)$ is the two-by-two identity matrix, and

$$\mathbf{A} \equiv \begin{pmatrix} \Omega_i^2 & J_{ij}^2 \\ J_{ji}^2 & \Omega_j^2 \end{pmatrix}. \quad (\text{F4})$$

Diagonalizing the matrix \mathbf{A} , we obtain the eigenvalues

$$\Omega_{\pm}^2 = \frac{\Omega_i^2 + \Omega_j^2}{2} \pm \sqrt{\frac{(\Omega_i^2 - \Omega_j^2)^2 + 4J_{ij}^4}{2}}, \quad (\text{F5})$$

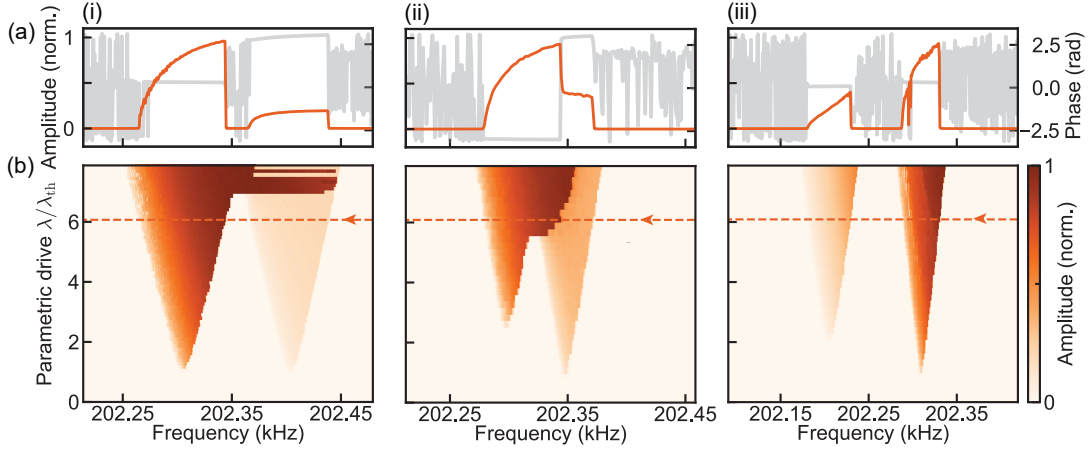


FIG. 9. Coupled parametric response of membranes 1 and 3. Columns (i)-(iii) correspond to three different values of \bar{U}_3 , cf. vertical lines in Fig. 8. (a) Parametric amplitude (orange) and phase (grey) responses measured on membrane 1 with $\lambda/\lambda_{\text{th}} = 6.1$ and $\bar{U}_1 = 34.1$ V. The frequency was swept from high to low values. (b) Response to parametric driving of the coupled membranes for various $\lambda/\lambda_{\text{th}}$. The sweeps in (a) were taken along the dashed orange lines.

with Ω_{\pm} corresponding to the frequencies of the eigenmodes, which have associated eigenvectors

$$\mathbf{x}_{\pm} = \pm \frac{1}{\sqrt{(\Omega_{\pm}^2 - \Omega_2^2)^2 + J_{ij}^4}} \begin{pmatrix} \Omega_{\pm}^2 - \Omega_2^2 \\ J_{ij}^2 \end{pmatrix}. \quad (\text{F6})$$

We find the normal mode frequencies at the avoided crossing, i.e. where $\Omega_i = \Omega_j$,

$$\Omega_{\pm} = \sqrt{\Omega_i^2 \pm J_{ij}^2} \approx \Omega_1 \pm \frac{J_{ij}^2}{2\Omega_i}, \quad (\text{F7})$$

in the limit of $\Omega_i \gg J_{ij}$. This leads to a normal-mode splitting

$$\Delta_{ij} = \Omega_+ - \Omega_- \approx \frac{J_{ij}^2}{\Omega_1}. \quad (\text{F8})$$

We can thus relate the fits of Ω_{\pm} , which yields J_{ij} , to the normal mode splitting.

At the crossing point, the eigenvectors are

$$x_{\pm} = x_1 \pm x_2 \quad (\text{F9})$$

with x_+ (x_-) corresponding to the symmetric (antisymmetric) mode with higher (lower) frequency. Note that a minus sign in front of coupling term $J_{ij}^2 x_j$ in Eq. (1) would instead translate to the higher frequency mode being antisymmetric. We verified with a wide-field (illuminating both membranes simultaneously) stroboscopic interferometer that the higher frequency mode is symmetric, confirming the sign we use in Eq. (1).

Appendix G: Coupling between membranes 1 and 3

In the main text, we demonstrate an avoided crossing between nearest-neighbor membranes 1 and 2, and their

coupled parametric responses when tuning their frequencies close to each other. Here, we repeat these measurements for membranes 1 and 3, which are diagonally connected.

Avoided crossing: As described in the main text, we measure the avoided crossing between membrane 1 and 3 by reading out membrane 1. We apply a voltage $\bar{U}_1 = 34.1$ V to membrane 1 and tune the frequency of membrane 3 by varying \bar{U}_3 , see Fig. 8. Fitting Eq. (4) to our data, we obtain coupling $J_{13}/2\pi = (2.77 \pm 0.03)$ kHz, leading to normal mode splitting $\Delta_{13}/2\pi = (37.9 \pm 0.4)$ Hz. As expected, this splitting is smaller than between membranes 1 and 2 since membranes 1 and 3 are further apart.

Tuning of Arnold tongues: We now measure the coupled parametric responses of membranes 1 and 3, see Fig. 9. We apply $\bar{U}_1 = 34.1$ V to membrane 1, and various \bar{U}_3 to membrane 3 corresponding to the vertical lines in Fig. 8. We apply a parametric drive λ to each membrane at frequency 2ω and read out the displacement x_1 of membrane 1 at ω , while we sweep ω from high to low frequencies. The same qualitative behavior as described in the main text can be observed.

Appendix H: Matching parametric drive strengths

In order to measure coupled Arnold tongues, we need to carefully tune the parametric drive voltage $\tilde{U}_{2\omega,i}$ applied each membrane. Since each membrane has a different DC voltage \bar{U}_i applied to it, and has a different quality factor Q_i , they require different AC voltage amplitudes to achieve the same parametric drive strength λ . This driving further needs to be tuned due to mode hybridization. In practice, we simply attenuate the AC voltage applied to one of the membrane $\tilde{U}_{2\omega,i}$. Driving at different parametric drive strengths results in vari-

ous artifacts and different phase diagrams. For instance, in Fig. 9(i)(b), we can observe such artifacts for sweeps

around λ/λ_{th} due to a slight discrepancy in parametric drives for each membrane.

-
- [1] S. H. Strogatz, Exploring complex networks, *Nature* **410**, 268 (2001).
 - [2] M. De Domenico, More is different in real-world multi-layer networks, *Nat. Phys.* **19**, 1247 (2023).
 - [3] S. N. Dorogovtsev, A. V. Goltsev, and J. F. Mendes, Critical phenomena in complex networks, *Rev. Mod. Phys.* **80**, 1275 (2008).
 - [4] J. J. Hopfield, Neural networks and physical systems with emergent collective computational abilities, *PNAS* **79**, 2554 (1982).
 - [5] N. Mohseni, P. L. McMahon, and T. Byrnes, Ising machines as hardware solvers of combinatorial optimization problems, *Nat. Rev. Phys.* **4**, 363 (2022).
 - [6] A. Arenas, A. Díaz-Guilera, J. Kurths, Y. Moreno, and C. Zhou, Synchronization in complex networks, *Phys. Rep.* **469**, 93 (2008).
 - [7] M. Scheffer, J. Bascompte, W. A. Brock, V. Brovkin, S. R. Carpenter, V. Dakos, H. Held, E. H. Van Nes, M. Rietkerk, and G. Sugihara, Early-warning signals for critical transitions, *Nature* **461**, 53 (2009).
 - [8] M. Scheffer, S. R. Carpenter, T. M. Lenton, J. Bascompte, W. Brock, V. Dakos, J. Van de Koppel, I. A. Van de Leemput, S. A. Levin, E. H. Van Nes, *et al.*, Anticipating critical transitions, *Science* **338**, 344 (2012).
 - [9] Z. Liu, X. Zhang, X. Ru, T.-T. Gao, J. M. Moore, and G. Yan, Early predictor for the onset of critical transitions in networked dynamical systems, *Phys. Rev. X* **14**, 031009 (2024).
 - [10] F. Grziwotz, C.-W. Chang, V. Dakos, E. H. van Nes, M. Schwarzländer, O. Kamps, M. Heßler, I. T. Tokuda, A. Telschow, and C.-h. Hsieh, Anticipating the occurrence and type of critical transitions, *Sci. Adv.* **9**, eabq4558 (2023).
 - [11] B. Harris, L. L. Gollo, and B. D. Fulcher, Tracking the distance to criticality in systems with unknown noise, *Phys. Rev. X* **14**, 031021 (2024).
 - [12] O. Artime, M. Grassia, M. De Domenico, J. P. Gleeson, H. A. Makse, G. Mangioni, M. Perc, and F. Radicchi, Robustness and resilience of complex networks, *Nat. Rev. Phys.* **6**, 114 (2024).
 - [13] D. M. Abrams and S. H. Strogatz, Chimera states for coupled oscillators, *Phys. Rev. Lett.* **93**, 174102 (2004).
 - [14] M. H. Matheny, J. Emenheiser, W. Fon, A. Chapman, A. Salova, M. Rohden, J. Li, M. Hudoba de Badyn, M. Pósfai, L. Duenas-Osorio, *et al.*, Exotic states in a simple network of nanoelectromechanical oscillators, *Science* **363**, eaav7932 (2019).
 - [15] M. C. Lifshitz, R. Cross, Nonlinear dynamics of nanomechanical and micromechanical resonators, in *Reviews of Nonlinear Dynamics and Complexity* (Wiley, 2009) pp. 1–52.
 - [16] A. Bachtold, J. Moser, and M. Dykman, Mesoscopic physics of nanomechanical systems, *Reviews of Modern Physics* **94**, 045005 (2022).
 - [17] M. Dykman, *Fluctuating Nonlinear Oscillators* (Oxford University Press, 2012).
 - [18] A. Eichler and O. Zilberberg, *Classical and Quantum Parametric Phenomena* (Oxford University Press, 2023).
 - [19] I. Mahboob and H. Yamaguchi, Bit storage and bit flip operations in an electromechanical oscillator, *Nat. Nano.* **3**, 275 (2008).
 - [20] C. M. Wilson, T. Duty, M. Sandberg, F. Persson, V. Shumeiko, and P. Delsing, Photon generation in an electromagnetic cavity with a time-dependent boundary, *Phys. Rev. Lett.* **105**, 233907 (2010).
 - [21] S. Puri, S. Boutin, and A. Blais, Engineering the quantum states of light in a kerr-nonlinear resonator by two-photon driving, *npj Quantum Information* **3**, 18 (2017).
 - [22] I. Mahboob, H. Okamoto, and H. Yamaguchi, An electromechanical ising hamiltonian, *Sci. Adv.* **2**, e1600236 (2016).
 - [23] S. E. Nigg, N. Lörch, and R. P. Tiwari, Robust quantum optimizer with full connectivity, *Sci. Adv.* **3**, e1602273 (2017).
 - [24] Z. Nosan, P. Märki, N. Hauff, C. Knaut, and A. Eichler, Gate-controlled phase switching in a parametron, *Phys. Rev. E* **99**, 062205 (2019).
 - [25] M. Frimmer, T. L. Heugel, Z. Nosan, F. Tebbenjohanns, D. Hälgl, A. Akin, C. L. Degen, L. Novotny, R. Chitra, O. Zilberberg, and A. Eichler, Rapid flipping of parametric phase states, *Phys. Rev. Lett.* **123**, 254102 (2019).
 - [26] A. Grimm, N. E. Frattini, S. Puri, S. O. Mundhada, S. Touzard, M. Mirrahimi, S. M. Girvin, S. Shankar, and M. H. Devoret, Stabilization and operation of a kerr-cat qubit, *Nature* **584**, 205 (2020).
 - [27] Z. Wang, M. Pechal, E. A. Wollack, P. Arrangoiz-Arriola, M. Gao, N. R. Lee, and A. H. Safavi-Naeini, Quantum dynamics of a few-photon parametric oscillator, *Phys. Rev. X* **9**, 021049 (2019).
 - [28] S. Puri, A. Grimm, P. Campagne-Ibarcq, A. Eickbusch, K. Noh, G. Roberts, L. Jiang, M. Mirrahimi, M. H. Devoret, and S. M. Girvin, Stabilized cat in a driven nonlinear cavity: A fault-tolerant error syndrome detector, *Phys. Rev. X* **9**, 041009 (2019).
 - [29] J. M. Miller, D. D. Shin, H.-K. Kwon, S. W. Shaw, and T. W. Kenny, Phase control of self-excited parametric resonators, *Phys. Rev. Applied* **12**, 044053 (2019).
 - [30] T. Yamaji, S. Masuda, A. Yamaguchi, T. Satoh, A. Morioka, Y. Igarashi, M. Shirane, and T. Yamamoto, Correlated oscillations in kerr parametric oscillators with tunable effective coupling, *Phys. Rev. Appl.* **20**, 014057 (2023).
 - [31] N. E. Frattini, R. G. Cortiñas, J. Venkatraman, X. Xiao, Q. Su, C. U. Lei, B. J. Chapman, V. R. Joshi, S. M. Girvin, R. J. Schoelkopf, S. Puri, and M. H. Devoret, Observation of pairwise level degeneracies and the quantum regime of the arrhenius law in a double-well parametric oscillator, *Phys. Rev. X* **14**, 031040 (2024).
 - [32] P. Álvarez, D. Pittilini, F. Miserocchi, S. Raamamurthy, G. Margiani, O. Ameye, J. Del Pino, O. Zilberberg, and A. Eichler, Biased ising model using two coupled kerr parametric oscillators with external force, *Phys. Rev. Lett.* **132**, 207401 (2024).

- [33] C. Han, M. Wang, B. Zhang, M. Dykman, and H. Chan, Coupled parametric oscillators: From disorder-induced current to asymmetric ising model, *Phys. Rev. Res.* **6**, 023162 (2024).
- [34] G. Margiani, O. Ameye, O. Zilberberg, and A. Eichler, Three strongly coupled kerr parametric oscillators forming a boltzmann machine, *arXiv:2504.04254* (2025).
- [35] S. Xue, M. Maghrebi, G. I. Mias, and C. Piermarocchi, Critical dynamics and cyclic memory retrieval in non-reciprocal hopfield networks, *arXiv:2501.00983* (2025).
- [36] A. Szedlak, G. Paternostro, and C. Piermarocchi, Control of asymmetric hopfield networks and application to cancer attractors, *PloS one* **9**, e105842 (2014).
- [37] A. J. Mendoza and J. S. Haas, Intrinsic sources and functional impacts of asymmetry at electrical synapses, *Eneuro* **9** (2022).
- [38] H. Goto, Bifurcation-based adiabatic quantum computation with a nonlinear oscillator network, *Sci. Rep.* **6**, 21686 (2016).
- [39] M. I. Dykman, C. Bruder, N. Lörch, and Y. Zhang, Interaction-induced time-symmetry breaking in driven quantum oscillators, *Phys. Rev. B* **98**, 195444 (2018).
- [40] G. Margiani, J. del Pino, T. L. Heugel, N. E. Bousse, S. Guerrero, T. W. Kenny, O. Zilberberg, D. Sabonis, and A. Eichler, Deterministic and stochastic sampling of two coupled kerr parametric oscillators, *Phys. Rev. Res.* **5**, L012029 (2023).
- [41] T. L. Heugel, O. Zilberberg, C. Marty, R. Chitra, and A. Eichler, Ising machines with strong bilinear coupling, *Phys. Rev. Research* **4**, 013149 (2022).
- [42] T. L. Heugel, R. Chitra, A. Eichler, and O. Zilberberg, Proliferation of unstable states and their impact on stochastic out-of-equilibrium dynamics, *arXiv:2307.13718* (2023).
- [43] O. Ameye, A. Eichler, and O. Zilberberg, The parametric instability landscape of coupled kerr parametric oscillators, *arXiv:2501.08793* (2025).
- [44] H. Goto, Z. Lin, and Y. Nakamura, Boltzmann sampling from the ising model using quantum heating of coupled nonlinear oscillators, *Sci. Rep.* **8**, 7154 (2018).
- [45] M. Fruchart, R. Hanai, P. B. Littlewood, and V. Vitelli, Non-reciprocal phase transitions, *Nature* **592**, 363 (2021).
- [46] X. Zhou, S. Venkatachalam, R. Zhou, H. Xu, A. Pokharel, A. Fefferman, M. Zaknoune, and E. Collin, High-q silicon nitride drum resonators strongly coupled to gates, *Nano Lett.* **21**, 5738 (2021).
- [47] S. Schmid, T. Bagci, E. Zeuthen, J. M. Taylor, P. K. Herring, M. C. Cassidy, C. M. Marcus, L. Guillermo Villanueva, B. Amato, A. Boisen, *et al.*, Single-layer graphene on silicon nitride micromembrane resonators, *J. Appl. Phys.* **115** (2014).
- [48] T. Bagci, a. Simonsen, S. Schmid, L. Villanueva, E. Zeuthen, J. Appel, J. Taylor, a. Sørensen, K. Usami, a. Schliesser, and E. Polzik, Optical detection of radio waves through a nanomechanical transducer., *Nature* **507** (2014).
- [49] D. Puglia, R. Odessey, P. S. Burns, N. Luhmann, S. Schmid, and A. P. Higginbotham, Room temperature, cavity-free capacitive strong coupling to mechanical motion, *Nano Lett.* **25**, 2749 (2025).
- [50] M. H. de Jong, M. A. ten Wolde, A. Cupertino, S. Gröblacher, P. G. Steeneken, and R. A. Norte, Mechanical dissipation by substrate-mode coupling in sin resonators, *Appl. Phys. Lett.* **121** (2022).
- [51] F. Correia, G. Jara-Schulz, G. Madiot, S. Barbay, and R. Braive, Coherent interferometric control of strongly-coupled nano-electromechanical resonators, *Comm. Phys.* **7**, 233 (2024).
- [52] G. Madiot, F. Correia, S. Barbay, and R. Braive, Bichromatic synchronized chaos in driven coupled electro-optomechanical nanoresonators, *Phys. Rev. A* **104**, 023525 (2021).
- [53] T. L. Heugel, A. Eichler, R. Chitra, and O. Zilberberg, The role of fluctuations in quantum and classical time crystals, *SciPost Phys. Core* **6**, 053 (2023).
- [54] J. A. Conway, J. V. Osborn, and J. D. Fowler, Stroboscopic imaging interferometer for mems performance measurement, *JMEMS* **16**, 668 (2007).
- [55] Y. Tsaturyan, A. Barg, E. Polzik, and A. Schliesser, Ultracoherent nanomechanical resonators via soft clamping and dissipation dilution, *Nat. Nano.* **12**, 776 (2017).
- [56] A. Mashaal, L. Stefan, A. Ranfagni, L. Catalini, I. Chernobrovkin, T. Capelle, E. C. Langman, and A. Schliesser, Strong thermomechanical noise squeezing stabilized by feedback, *Phys. Rev. Research* **7**, L012071 (2025).
- [57] D. Smirnova, D. Leykam, Y. Chong, and Y. Kivshar, Nonlinear topological photonics, *Appl. Phys. Rev.* **7** (2020).
- [58] S. Ravets, N. Pernet, N. Mostaan, N. Goldman, and J. Bloch, Thouless pumping in a driven-dissipative kerr resonator array, *Phys. Rev. Lett.* **134**, 093801 (2025).
- [59] G. Villa, J. del Pino, V. Dumont, G. Rastelli, M. Michałek, A. Eichler, and O. Zilberberg, Topological classification of driven-dissipative nonlinear systems, *arXiv:2406.16591* (2024).
- [60] CRC Handbook, *CRC Handbook of Chemistry and Physics, 88th Edition*, 88th ed. (CRC Press, 2007).
- [61] B. Hauer, C. Doolin, K. Beach, and J. Davis, A general procedure for thermomechanical calibration of nano/micro-mechanical resonators, *Ann. Phys.* **339**, 181 (2013).
- [62] S. Schmid, L. G. Villanueva, and M. L. Roukes, *Fundamentals of nanomechanical resonators*, Vol. 49 (Springer, 2016).
- [63] A. Eichler, J. Moser, M. Dykman, and A. Bachtold, Symmetry breaking in a mechanical resonator made from a carbon nanotube, *Nat. Comm.* **4**, 2843 (2013).
- [64] I. Kozinsky, H. Postma, I. Bargatin, and M. Roukes, Tuning nonlinearity, dynamic range, and frequency of nanomechanical resonators, *Appl. Phys. Lett.* **88** (2006).
- [65] R. Lifshitz and M. C. Cross, Nonlinear dynamics of nanomechanical and micromechanical resonators, *Reviews of nonlinear dynamics and complexity* **1** (2008).
- [66] J. Thompson, B. Zwickl, A. Jayich, F. Marquardt, S. Girvin, and J. Harris, Strong dispersive coupling of a high-finesse cavity to a micromechanical membrane, *Nature* **452**, 72 (2008).
- [67] A. Jayich, J. Sankey, B. Zwickl, C. Yang, J. Thompson, S. Girvin, A. A. Clerk, F. Marquardt, and J. Harris, Dispersive optomechanics: a membrane inside a cavity, *New J. Phys.* **10**, 095008 (2008).
- [68] V. Dumont, S. Bernard, C. Reinhardt, A. Kato, M. Ruf, and J. C. Sankey, Flexure-tuned membrane-at-the-edge optomechanical system, *Opt. Exp.* **27**, 25731 (2019).